P H Y S I C A L   R E V I E W   L E T T E R S

Ferroelectric-Domain-Patterning-Controlled Schottky Junction State in Monolayer MoS$_2$

Zhiyong Xiao,[1,2] Jingfeng Song,[1,2] David K. Ferry,[3] Stephen Ducharme,[1,2] and Xia Hong[1,2,*]

[1]*Department of Physics and Astronomy, University of Nebraska-Lincoln, Nebraska 68588-0299, USA*
[2]*Nebraska Center for Materials and Nanoscience, University of Nebraska-Lincoln, Nebraska 68588-0299, USA*
[3]*School of Electrical, Computer, and Energy Engineering, Arizona State University, Tempe, Arizona 85287-5706, USA*
(Received 9 September 2016; published 8 June 2017)

We exploit scanning-probe-controlled domain patterning in a ferroelectric top layer to induce nonvolatile modulation of the conduction characteristic of monolayer MoS$_2$ between a transistor and a junction state. In the presence of a domain wall, MoS$_2$ exhibits rectified *I-V* characteristics that are well described by the thermionic emission model. The induced Schottky barrier height Φ_B^{eff} varies from 0.38 to 0.57 eV and is tunable by a SiO$_2$ global back gate, while the tuning range of Φ_B^{eff} depends sensitively on the conduction-band-tail trapping states. Our work points to a new route to achieving programmable functionalities in van der Waals materials and sheds light on the critical performance limiting factors in these hybrid systems.

Monolayer (ML) transition-metal dichalcogenide (TMDC) MX_2 ($M =$ Mo, W; $X =$ S, Se, Te) possesses atomic thickness, highly tunable electronic states, and direct band gaps of 1–2 eV [1], making them a versatile playground for imposing nanoscale band structure design [2] and building novel homo- and heterojunctions for nanoelectronic [3–6] and optoelectronic applications [7–9]. TMDC-based Schottky and *p-n* junctions have previously been achieved by exploiting multiple local gates [9,10], electric-double-layer gating controlled bipolar carrier injection [11], contact work function engineering [12,13], or exploring van der Waals heterostructures [14–16], where the device functionalities cannot be altered after fabrication. On the other hand, the ability to create well-defined but reconfigurable potential barriers at the nanoscale can be utilized to disentangle the intricate interplay of various impurity sources and the dielectric environment in determining the electronic and optical response of TMDC in the junction state, as well as achieving multifunctional operations on a single two-dimensional (2D) platform.

A promising approach to locally defining the potential profile and producing a programmable junction state in TMDCs is to capitalize on the nonvolatile, switchable polarization field of a ferroelectric gate. The ferroelectric field effect has previously been intensively investigated in layered van der Waals materials such as graphene and TMDCs for building novel logic and memory devices [17–20], tunnel junctions [21], sensors [22–24], and plasmonic and optoelectronic applications [25–28]. However, the unique opportunity offered by nanoscale polarization control, which can lead to local carrier density modulation in the 2D channel, has yet to be explored. In this study, employing domain patterning in an ultrathin ferroelectric polymer top layer via scanning probe microscopy, we have achieved for the first time programmable transistor and Schottky junction states in a single channel of ML MoS$_2$. In the monodomain states, we observed an Ohmic

source-drain current-voltage (I_{DS}-V_{DS}) relation for both the polarization up (P_{up}) and down (P_{down}) states. Modeling the transfer characteristics shows that the free electron band mobility of the sample is limited by charged impurity (CI) scattering, which is not affected by polarization switching. In the presence of a ferroelectric domain wall (DW) perpendicular to the current direction (denoted as the half P_{up}–half P_{down} state), the channel exhibits rectified *I-V* relation that can be well described by the thermionic emission model, with the induced Schottky barrier height Φ_B^{eff} further tunable by a SiO$_2$ global back gate.

We fabricated ML MoS$_2$ field effect transistor (FET) devices sandwiched between a 300 nm SiO$_2$ global back gate and a ferroelectric top layer (17.8 $\pm$ 0.7 nm) of poly(vinylidene fluoride-trifluoroethylene) [P(VDF-TrFE)] [Fig. 1(a)], where the copolymer film was deposited using the Langmuir-Blodgett (LB) technique [29–31]. Unlike the thick P(VDF-TrFE) films prepared by spin coating [17,18,22,26], the ultrathin LB films possess smooth surfaces (∼1 nm surface roughness) and low coercive voltage (<10 V), making it possible to write and image ferroelectric domains with nanoscale precision via the conductive probe atomic force microscopy (AFM) and piezoresponse force microscopy (PFM) [37,38]. The reported electrical results were based on 6 MoS$_2$ samples, denoted as D1–D6.

Figure 1(b) shows the room-temperature transfer characteristic of sample D2 gated through SiO$_2$ [Fig. 1(c)]. With increasing back gate voltage V_{BG}, I_{DS} exhibits an exponential growth at low V_{BG} followed by a quasilinear gate dependence beyond a transition voltage (denoted as V_t), signaling the shift of the Fermi level E_F from well residing in the band gap to close to the conduction-band edge. We extracted the field effect mobility of the sample from the linear region of $I_{DS}(V_{\mathrm{BG}})$ as $\mu_{\mathrm{FE}} = (1/e\gamma)(L/W)$ (dG/dV_{BG}), where $\gamma = 7.2 \times 10^{10}$ cm^{-2} V^{-1} is the gating efficiency of 300 nm SiO$_2$, $G = I_{DS}/V_{DS}$ is the channel conductance, and L (W) is the channel length (width).
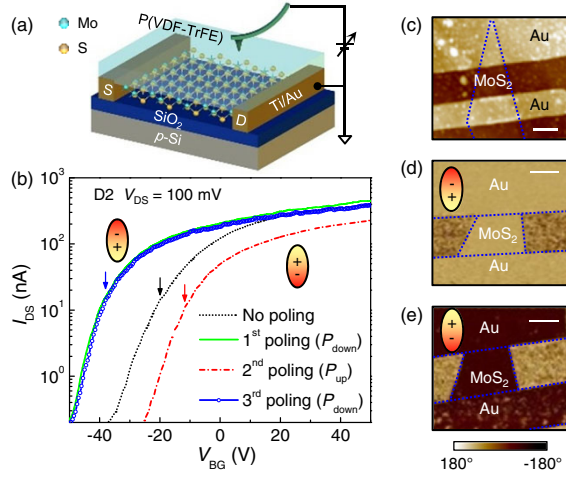
FIG. 1. (a) Device schematic. (b) Room-temperature transfer characteristics for sample D2 in the initial no poling state, and after writing P(VDF-TrFE) with +10 V (1st poling), −10 V (2nd poling), and +10 V (3rd poling) tip bias. The arrows mark the corresponding V_t's. (c) The AFM topography image of the sample and the PFM phase images after (d) the 1st and (e) 2nd poling. The scale bars are 1 μm. The dotted lines outline the MoS$_2$ flake and the Au electrodes.

As there is no metal electrode on P(VDF-TrFE), the presence of the ferroelectric top layer does not change γ, as demonstrated in previous studies of SiO$_2$-gate graphene with ice [39] and HfO$_2$ [40] top layers. In the as-deposited state, the sample exhibits μ_{FE} of 6.7 cm^2 V^{-1} s^{-1} and V_t of −20 V.

To control the out-of-plane polarization of the copolymer, we apply a constant bias voltage higher than the coercive voltage to a conductive AFM tip while it is scanning on the sample surface in the contact mode [Fig. 1(a)]. We first switched the copolymer to the uniform P_{down} state by writing the entire channel area with a tip bias V_{tip} of +10 V while keeping MoS$_2$ grounded. The PFM phase image [Fig. 1(d)] shows that P(VDF-TrFE) on top of the device area has been uniformly polarized, while the portion on top of the SiO$_2$ substrate remains unpoled. In the P_{down} state, electrons are accumulated in MoS$_2$, which shifts E_F towards the conduction-band edge, yielding a nonvolatile offset in the doping level. The resulting transfer curve shifts to the negative V_{BG} direction, with corresponding μ_{FE} of 4.7 cm^2 V^{-1} s^{-1} and V_t of −38 V.

We then polarized the ferroelectric top layer to the uniform P_{up} state [Fig. 1(e)] by scanning the entire sample area with $V_{tip} = -10$ V, depleting electrons from MoS$_2$. The resulting I_{DS}-V_{BG} curve shifts to the positive V_{BG} direction with $V_t = -12$ V. The slightly lower μ_{FE} of 3.3 cm^2 V^{-1} s^{-1} is due to the reduced screening of CIs in the depletion state. The scanning probe controlled polarization switching is nonvolatile and fully reversible. The third AFM writing with $V_{tip} = +10$ V poled the copolymer back to the uniform P_{down} state, and the resulting transfer

curve of MoS$_2$ overlaps with that of the first poling. The switching ratio between the high (P_{down}) and low (P_{up}) conductance states reaches ∼450 at $V_{BG} = -25$ V.

In previous studies of ferroelectric-gated TMDC, despite the tremendous progress in developing various nanoelectronic or optoelectronic devices [17–22,25,26], in-depth understanding is yet to be gained on how the ferroelectric layer affects the mobility of the TMDC channel, e.g., regarding the presence of a charged interface, the remote interfacial polar (RIP) phonon, and the polarization reversal. To assess these ferroelectric-specific factors, we have quantitatively modeled the transfer characteristics of MoS$_2$ in both polarization states. The temperature dependence of I_{DS} shows that E_F for both polarization states lies in the band gap (E_g) for the entire gating range [31]. It is thus important to consider in the modeling the conduction-band-tail trapping states within the gap region as well as the localized states above the conduction-band edge, which have been attributed to the charged impurities such as S vacancies in MoS$_2$ and CIs from the dielectric environment [6]. To account for these midgap states, we incorporated the density of states (DOS) distribution in MoS$_2$ proposed in Ref. [6]:

$$D_n(E) = \begin{cases} \alpha D_0 \exp[-\frac{E-E_D}{\varphi}], & E_D - \frac{E_g}{2} < E < E_D, \\ D_0 - (1-\alpha)D_0 \exp[-\frac{E-E_D}{\varphi'}], & E > E_D \end{cases}.$$

$$(1)$$

Here $D_0 \sim 3.9 \times 10^{14}$ eV^{-1} cm^{-2} is the 2D DOS for crystalline MoS$_2$, E_D is the conduction-band edge, φ is the characteristic depth of the band tail, and α and φ' are fitting parameters. Using Eq. (1), we first modeled the V_{BG} dependence of the total carrier density n_{total} and the free electron density n_{free} for sample D3 in both polarization states at $V_{BG} > V_t$ [Fig. 2(a)] [31]. Here n_{total} includes both trapped and localized electrons and n_{free}, with $\Delta n_{total} = \gamma \Delta V_{BG}$. For n_{free}, we only consider the extended states above the mobility edge energy E_M with respect to the conduction-band edge:

$$n_{free}(300 \text{ K}) = \int_{E_M}^{\infty} D_n(E) f(E, 300 \text{ K}) \, dE, \quad (2)$$

where $D_n(E)$ is given by Eq. (1) and $f(E)$ is the Fermi-Dirac distribution. We used the parameters of $\varphi = 110$ meV and $E_M = 10$ meV similar to those reported in Ref. [6], as our samples possess similar mobility values.

Figure 2(b) shows the free electron band mobility $\mu_{band} = \sigma/n_{free}e$ as a function of n_{free}, which reveals two important points. First, even though the field effect mobility in this region is a constant [i.e., $I_{DS}(V_{BG})$ is linear], the band mobility associated with the free electrons actually increases linearly with increasing n_{free} for both polarization states, reaching ∼10 cm^2 V^{-1} s^{-1} at $n = 1 \times 10^{11}$ cm^{-2}.
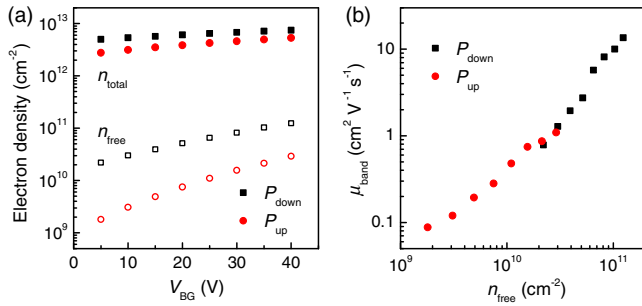
FIG. 2. (a) Calculated n_{total} (solid symbols) and n_{free} (open symbols) as a function of V_{BG} for sample D3 at $V_{BG} > V_t$ for both polarization states, and (b) the corresponding μ_{band} as a function of n_{free}.

This suggests CI scattering rather than phonon scattering as the dominant mobility limiting mechanism [41], since the increased density can enhance the screening of the CIs, resulting in higher mobility. Using Boltzmann transport theory with relaxation time approximation, we find this mobility level corresponds to a CI density $N_i \sim 3 \times 10^{12} cm^{-2}$ [31], comparable with the value obtained in MoS$_2$ sandwiched between SiO$_2$ and HfO$_2$ [4]. It further confirms that the parameters for the band tail states and mobility edge in Ref. [6] can give a reasonable description of the charge trapping or localization in our samples. Our device mobility extracted from the gap region is also consistent with the high density mobility values reported in literature for MoS$_2$ on SiO$_2$ [6,42–44], as discussed in the Supplemental Material [31]. At this low density range, scattering from intrinsic acoustic and nonpolar optical phonons in MoS$_2$ is negligibly small. Despite the high dielectric constant of P(VDF-TrFE) ($\varepsilon_{PVDF} = 10$), its RIP phonon also does not play a critical role in limiting the mobility of MoS$_2$, in stark contrast with other high-k dielectrics such as HfO$_2$ and Al$_2$O$_3$ [41]. While P(VDF-TrFE) can provide effective dielectric screening to the RIP modes of SiO$_2$, its most active optical phonon modes are at $\hbar\omega = 63$ and 109 meV [45], and the corresponding RIP modes would not contribute as strongly as that of SiO$_2$ at room temperature [46]. Second, at the same n_{free}, the sample possesses similar mobility values for both polarization states, indicating that switching the polarization direction does not introduce additional scatterers. This is understandable since the switchable polarization originates from the crystalline fraction of P(VDF-TrFE), which imposes a periodic polarization field that does not scatter electrons.

We next explored the possibility of creating a potential barrier in the MoS$_2$ channel by writing a ferroelectric DW perpendicular to the current direction. In the monodomain states, despite the large current modulation, we observe linear, Ohmic-like I_{DS}-V_{DS} characteristics for both polarization states within $V_{DS} = \pm 100$ mV [Fig. 3(a)] over the entire V_{BG} range for all samples investigated. In sharp contrast, when P(VDF-TrFE) was patterned into two
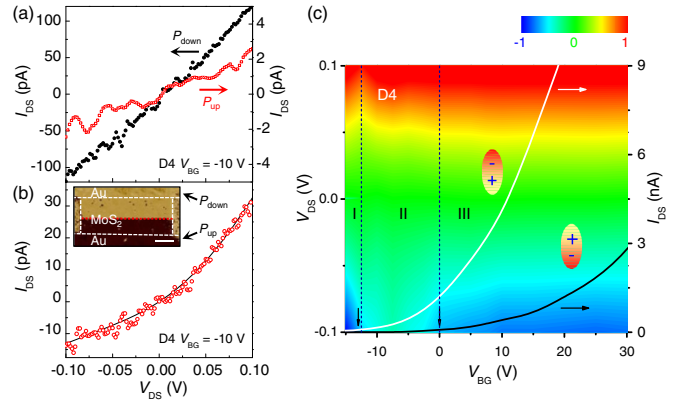

FIG. 3. (a) Room-temperature $I_{DS}(V_{DS})$ of sample D4 at $V_{BG} = -10$ V for the monodomain states, and (b) the half P_{up}–half P_{down} state (open symbols) with a fit to Eq. (3) (solid line). Inset: PFM phase image of the domain structure. Scale bar: 1 μm. (c) Normalized I_{DS} vs V_{DS} and V_{BG} for the half P_{up}–half P_{down} state. Superimposed on the plot are the transfer curves at $V_{DS} = 100$ mV for the uniform P_{up} and P_{down} states (right axis). The vertical arrows mark the V_t. The dashed lines mark the boundaries separating regions I, II, and III.

domains with opposite out-of-plane polarization directions [Fig. 3(b) inset], at the same V_{BG} of -10 V, sample D4 exhibits rectified nonlinear conduction with much weaker variation in I_{DS} at reverse bias [Fig. 3(b)]. Such nonlinearity can be further tuned by V_{BG}. Figure 3(c) shows the color contour of I_{DS} normalized to the value at $V_{DS} = +100$ mV vs V_{DS} and V_{BG} for this sample, which exhibits a clear evolution between two distinct behaviors with increasing V_{BG}. At low V_{BG} (region I: $V_{BG} < -12.5$ V), we observe a linear Ohmic-like I_{DS}-V_{DS} relation. At the intermediate V_{BG} range (region II: $-12.5 V \leq V_{BG} \leq 0$ V), I_{DS} exhibits the rectified, diodelike I_{DS}-V_{DS} behavior. Further increasing V_{BG} to region III recovers the linear conduction.

To understand the origin of the evolved I_{DS}-V_{DS} characteristics, we superimposed on Fig. 3(c) the transfer curves of this sample in the monodomain states. The corresponding transition voltages are $V_t = -13$ V for P_{down} and $V_t = 0$ V for the P_{up} state, which are in excellent agreement with the boundary V_{BG} voltages that separate regions I, II, and III, suggesting that it is the band alignment between the P_{up} and P_{down} sides of the channel that determines the conduction characteristic. When the sample is gated into region I, E_F for both sides is deep in the gap region, leading to high channel resistance. We expect an intrinsic to the n-doped type interface, and the channel conduction can be modeled as two resistors R_{down} and R_{up}, corresponding to the P_{down} and P_{up} domains, respectively, in series connection. In region II, E_F for the P_{down} side of the channel is approaching the conduction-band edge, so MoS$_2$ is doped with a high density of free electrons in the extended states at room temperature, while the P_{up} side of the channel remains in the semiconducting state. We thus expect a Schottky junction forming
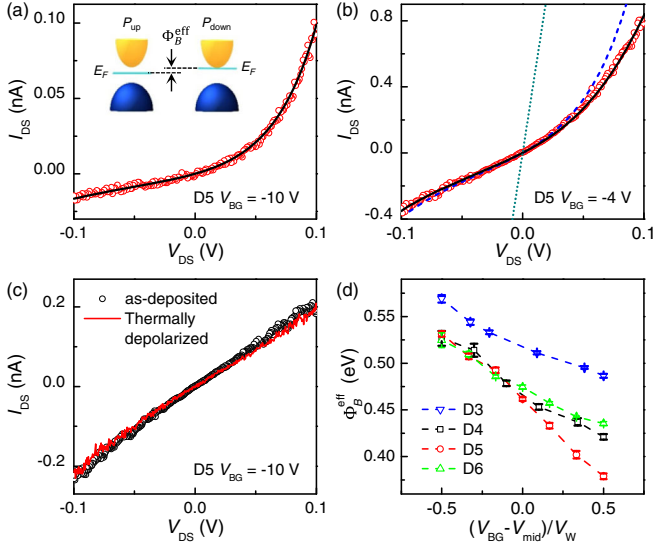
FIG. 4.   (a) $I_{DS}(V_{DS})$ (open symbols) at $V_{BG} = -10$ V with a fit to Eq. (3) (solid line). Inset: Schematic band diagram for MoS$_2$ in the P_{up} and P_{down} states. (b) $I_{DS}(V_{DS})$ (open symbols) at $V_{BG} = -4$ V with a fit to Eq. (4) (solid line). The dashed and dotted lines correspond to the first and second terms in Eq. (4), respectively. (c) $I_{DS}(V_{DS})$ at $V_{BG} = -10$ V taken in the as-prepared state of P(VDF-TrFE) (black symbols) and after domain patterning and thermal depolarization (red line). (d) Φ_B^{eff} as a function of normalized V_{BG} for samples D3–D6.

in the vicinity of the DW, with the effective barrier height Φ_B^{eff} corresponding to the difference in E_F between the P_{up} and P_{down} sides [Fig. 4(a) inset]. Similarly, well within region III, both sides of the channel are doped with high densities of electrons, yielding low channel resistance with linear conduction.

In region II, we need to consider the additional junction contribution in series connection with R_{up} and R_{down} to model the total channel conduction. We quantitatively modeled the rectified I-V behavior in region II using the thermionic emission model [13,47]:

$$I_{DS} = A_{2D}^* T^{3/2} W \exp\left(-\frac{e\Phi_B^{eff}}{k_B T}\right) \exp\left(\frac{eV_{DS}}{nk_B T}\right)$$
$$\times \left[1 - \exp\left(-\frac{eV_{DS}}{k_B T}\right)\right], \qquad (3)$$

with $A_{2D}^* = [(eM_c k_B^{3/2})/(\pi \hbar^2)](m_t^*/2\pi)^{1/2}$, where W is the width of the conduction channel, n is the ideality factor, which is normally between 1 and 2, and $m_t^* = 0.45m_0$ is the transverse electron effective mass for ML MoS$_2$ [3]. Here A_{2D}^* is the 2D effective Richardson constant, with the number of equivalent conduction-band minima $M_c = 2$. Figures 4(a)–4(b) show the I_{DS}-V_{DS} curves taken on sample D5 in region II (between $V_{BG} = -12$ and 0 V for this sample). At $V_{BG} = -10$ V, the channel conduction can be well described by Eq. (3) with $\Phi_B^{eff} = 0.51$ eV, which can be further tuned by V_{BG}. The domain-patterning-induced

junction states have been observed in all four samples investigated (D3–D6), with the ideality factor n ranging from 1.4 to 1.8, consistent with previously reported results [9,12].

The fact that Eq. (3) can give an accurate description of the conduction characteristic indicates that the resistive contribution of R_{down} and R_{up} is also absent at $V_{BG} = -10$ V. As MoS$_2$ exhibits more than 1 order of magnitude change in conductance between the two polarization states in region II [Figs. 1(b) and 3], it is reasonable to neglect R_{down}. The absence of R_{up}, on the other hand, suggests that the extension of the junction transition region is comparable with or larger than the P_{up} side channel length at low carrier density. At sufficiently high V_{BG} ($V_{BG} \geq -6$ V), when the junction width decreases with increasing carrier density and becomes shorter than the associated channel length, Eq. (3) can no longer provide a satisfactory fit to the I_{DS}-V_{DS} relation. Rather, the conduction has to be modeled as a Schottky junction in series connection with a resistor [31]:

$$V'_{DS} = V_{DS}(I_{DS}) + I_{DS}R_{up}, \qquad (4)$$

where $V_{DS}(I_{DS})$ is defined by Eq. (3). Figure 4(b) shows the fit for the I_{DS}-V_{DS} curve at $V_{BG} = -4$ V to this model, where the first term yields a barrier height of $\Phi_B^{eff} = 0.43$ eV. Comparing the extracted R_{up} with the channel resistance in the uniform P_{up} state yields a channel length of 23 nm, much shorter than the associated P_{up} domain length (350 nm), confirming that on the P_{up} side the junction transition region extends well beyond the vicinity of the DW.

As a control experiment, we erased the domain structure by thermally heating the sample in vacuum to 80 °C, close to its Curie temperature, for 2 h. The copolymer film then recovers its as-deposited state with polarization randomly oriented, which can be attributed to its low DW energy [38]. After thermal depolarization, the I_{DS}-V_{DS} curve at $V_{BG} = -10$ V agrees well with the linear behavior in the as-deposited state [Fig. 4(c)], indicating that the observed junction state is resulting from the ferroelectric domain patterning and the sample quality is preserved during the polarization switching.

As the Schottky barrier height Φ_B^{eff} is defined by the band alignment between the P_{down} and P_{up} states [Fig. 4(a) inset], it can be further tuned by V_{BG}. Figure 4(d) shows Φ_B^{eff} as a function of the normalized back gate voltage $(V_{BG} - V_{mid})/V_W$ for samples D3–D6, where V_{mid} and V_W are the middle point and width of region II, respectively. All samples exhibit consistent V_{BG} dependence of Φ_B^{eff}, which decreases with increasing V_{BG} by 90–150 meV. This reduction in Φ_B^{eff} is a consequence of the high density of states close to the MoS$_2$ conduction-band edge, which results in a moderate change of E_F on the P_{down} side where the sample is doped close to the conduction-band.

At the low-V_{BG} end of region III, close to the boundary with region II, the channel conduction still exhibits slight nonlinearity but can no longer be properly modeled by Eq. (4) [31], even though the P_{up} state E_F is still about 0.4–0.5 eV below the extended states [Fig. 4(d)]. This can be well explained by the band tail states described by Eq. (1), which would limit the gate-tunable range of Φ_B^{eff}, or the width of region II (V_W). As shown in Ref. [6], these impurity states can extend to up to 0.4–0.5 eV below the conduction-band of MoS_2, and can contribute to hopping-type conduction, which naturally explains the lack of a well-defined energy barrier at this gating range. Overall, a range of Φ_B^{eff} from 0.38 to 0.57 eV has been realized in our samples [Fig. 4(d)].

In conclusion, we have demonstrated that nanoscale ferroelectric domain patterning can be utilized to reversibly tune the functionality of a 2D channel, while polarization switching does not have a pronounced impact on the channel mobility. This approach can be applied to a wide range of van der Waals materials to design various homojunctions and nanostructures, such as nanoribbons, nanodots, and super-lattices. Compared to the lithographical methods, the non-volatile field effect allows one to impose different functional designs on the same 2D channel without introducing dis-ordered interface or edge states. It also opens up the opportunity to integrate logic, memory, and photovoltaic functionalities in a single material platform for nanoelec-tronic and optoelectronic applications.

---

*Corresponding author.
xia.hong@unl.edu

[1] Q. H. Wang, K. Kalantar-Zadeh, A. Kis, J. N. Coleman, and M. S. Strano, Electronics and optoelectronics of two-dimensional transition metal dichalcogenides, Nat. Nanotechnol. **7**, 699 (2012).

[2] A. K. Geim and I. V. Grigorieva, van der Waals hetero-structures, Nature **499**, 419 (2013).

[3] Y. Yoon, K. Ganapathi, and S. Salahuddin, How good can monolayer MoS_2 transistors Be?, Nano Lett. **11**, 3768 (2011).

[4] B. Radisavljevic, A. Radenovic, J. Brivio, V. Giacometti, and A. Kis, Single-layer MoS_2 transistors, Nat. Nanotechnol. **6**, 147 (2011).

[5] D. Jariwala, V. K. Sangwan, L. J. Lauhon, T. J. Marks, and M. C. Hersam, Emerging device applications for semiconducting two-dimensional transition metal dichalcogenides, ACS Nano **8**, 1102 (2014).

[6] W. J. Zhu, T. Low, Y. H. Lee, H. Wang, D. B. Farmer, J. Kong, F. N. Xia, and P. Avouris, Electronic transport and device prospects of monolayer molybdenum disulphide grown by chemical vapour deposition, Nat. Commun. **5**, 3087 (2014).

[7] Z. Yin, H. Li, H. Li, L. Jiang, Y. Shi, Y. Sun, G. Lu, Q. Zhang, X. Chen, and H. Zhang, Single-layer MoS_2 phototransistors, ACS Nano **6**, 74 (2012).

[8] F. H. L. Koppens, T. Mueller, P. Avouris, A. C. Ferrari, M. S. Vitiello, and M. Polini, Photodetectors based on graphene, other two-dimensional materials and hybrid systems, Nat. Nanotechnol. **9**, 780 (2014).

[9] B. W. H. Baugher, H. O. H. Churchill, Y. F. Yang, and P. Jarillo-Herrero, Optoelectronic devices based on electrically tunable p-n diodes in a monolayer dichalcogenide, Nat. Nanotechnol. **9**, 262 (2014).

[10] D. J. Groenendijk, M. Buscema, G. A. Steele, S. M. de Vasconcellos, R. Bratschitsch, H. S. J. van der Zant, and A. Castellanos-Gomez, Photovoltaic and photothermoelectric effect in a double-gated WSe_2 device, Nano Lett. **14**, 5846 (2014).

[11] S. Jo, N. Ubrig, H. Berger, A. B. Kuzmenko, and A. F. Morpurgo, Mono- and bilayer WS_2 light-emitting transistors, Nano Lett. **14**, 2019 (2014).

[12] S. Chuang, C. Battaglia, A. Azcatl, S. McDonnell, J. S. Kang, X. Yin, M. Tosun, R. Kapadia, H. Fang, R. M. Wallace, and A. Javey, MoS_2 P-type transistors and diodes enabled by high work function MoO_x contacts, Nano Lett. **14**, 1337 (2014).

[13] J. Wang, D. Rhodes, S. Feng, M. A. T. Nguyen, K. Watanabe, T. Taniguchi, T. E. Mallouk, M. Terrones, L. Balicas, and J. Zhu, Gate-modulated conductance of few-layer WSe_2 field-effect transistors in the subgap regime: Schottky barrier transistor and subgap impurity states, Appl. Phys. Lett. **106**, 152104 (2015).

[14] C. H. Lee, G. H. Lee, A. M. van der Zande, W. C. Chen, Y. L. Li, M. Y. Han, X. Cui, G. Arefe, C. Nuckolls, T. F. Heinz, J. Guo, J. Hone, and P. Kim, Atomically thin p-n junctions with van der Waals heterointerfaces, Nat. Nanotechnol. **9**, 676 (2014).

[15] Y. X. Deng, Z. Luo, N. J. Conrad, H. Liu, Y. J. Gong, S. Najmaei, P. M. Ajayan, J. Lou, X. F. Xu, and P. D. Ye, Black phosphorus-monolayer MoS_2 van der Waals heterojunction p-n diode, ACS Nano **8**, 8292 (2014).

[16] F. Withers, O. Del Pozo-Zamudio, A. Mishchenko, A. P. Rooney, A. Gholinia, K. Watanabe, T. Taniguchi, S. J. Haigh, A. K. Geim, A. I. Tartakovskii, and K. S. Novoselov, Light-emitting diodes by band-structure engineering in van der Waals heterostructures, Nat. Mater. **14**, 301 (2015).

[17] X. Hong, Emerging ferroelectric transistors with nanoscale channel materials: the possibilities, the limitations, J. Phys. Condens. Matter **28**, 103003 (2016).

[18] H. S. Lee, S. W. Min, M. K. Park, Y. T. Lee, P. J. Jeon, J. H. Kim, S. Ryu, and S. Im, MoS_2 nanosheets for top-gate nonvolatile memory transistor channel, Small **8**, 3111 (2012).

[19] A. Nguyen, P. Sharma, T. Scott, E. Preciado, V. Klee, D. Sun, I. H. D. Lu, D. Barroso, S. Kim, V. Y. Shur, A. R. Akhmatkhanov, A. Gruverman, L. Bartels, and P. A. Dowben, Toward ferroelectric control of monolayer MoS_2, Nano Lett. **15**, 3364 (2015).

[20] C. Zhou, X. Wang, S. Raju, Z. Lin, D. Villaroman, B. Huang, H. L. -W. Chan, M. Chan, and Y. Chai, Low voltage and high ON/OFF ratio field-effect transistors based on CVD MoS_2 and ultra high-k gate dielectric PZT, Nanoscale **7**, 8695 (2015).

[21] H. Lu, A. Lipatov, S. Ryu, D. J. Kim, H. Lee, M. Y. Zhuravlev, C. B. Eom, E. Y. Tsymbal, A. Sinitskii, and A. Gruverman, Ferroelectric tunnel junctions with graphene electrodes, Nat. Commun. **5**, 5518 (2014).

[22] W. Park, J. H. Yang, C. G. Kang, Y. G. Lee, H. J. Hwang, C. Cho, S. K. Lim, S. C. Kang, W. K. Hong, S. K. Lee, S. Lee, and B. H. Lee, Characteristics of a pressure sensitive touch sensor using a piezoelectric PVDF-TrFE/MoS_2 stack, Nanotechnology **24**, 475501 (2013).

[23] A. Rajapitamahuni, J. Hoffman, C. H. Ahn, and X. Hong, Examining graphene field effect sensors for ferroelectric thin film studies, Nano Lett. **13**, 4374 (2013).

[24] C. Ma, Y. Gong, R. Lu, E. Brown, B. Ma, J. Li, and J. Wu, Detangling extrinsic and intrinsic hysteresis for detecting dynamic switch of electric dipoles using graphene field-effect transistors on ferroelectric gates, Nanoscale **7**, 18489 (2015).

[25] A. Lipatov, P. Sharma, A. Gruverman, and A. Sinitskii, Optoelectrical molybdenum disulfide (MoS_2)—ferroelectric memories, ACS Nano **9**, 8089 (2015).

[26] X. Wang, P. Wang, J. Wang, W. Hu, X. Zhou, N. Guo, H. Huang, S. Sun, H. Shen, T. Lin, M. Tang, L. Liao, A. Jiang, J. Sun, X. Meng, X. Chen, W. Lu, and J. Chu, Ultrasensitive and broadband MoS_2 photodetector driven by ferroelectrics, Adv. Mater. **27**, 6575 (2015).

[27] M. D. Goldflam, G.-X. Ni, K. W. Post, Z. Fei, Y. Yeo, J. Y. Tan, A. S. Rodin, B. C. Chapler, B. Özyilmaz, A. H. Castro Neto, M. M. Fogler, and D. N. Basov, Tuning and persistent switching of graphene plasmons on a ferroelectric substrate, Nano Lett. **15**, 4859 (2015).

[28] C. H. Li, K. M. McCreary, and B. T. Jonker, Spatial control of photoluminescence at room temperature by ferroelectric domains in monolayer WS_2/PZT hybrid structures, ACS Omega **1**, 1075 (2016).

[29] S. Ducharme, S. P. Palto, V. M. Freidkin, and L. M. Blinov, in *Handbook of Thin Film Materials*, edited by H. S. Nalwa (Academic, San Diego, 2002), Chap. 11.

[30] M. J. Bai, A. V. Sorokin, D. W. Thompson, M. Poulsen, S. Ducharme, C. M. Herzinger, S. Palto, V. M. Fridkin, S. G. Yudin, V. E. Savchenko, and L. K. Gribova, Determination of the optical dispersion in ferroelectric vinylidene fluoride (70%)/trifluoroethylene (30%) copolymer Langmuir-Blodgett films, J. Appl. Phys. **95**, 3372 (2004).

[31] See Supplemental Material at http://link.aps.org/supplemental/10.1103/PhysRevLett.118.236801 for the details on sample preparation, electrical characterization, and data modeling, which include Refs. [32–36].

[32] C. Lee, H. Yan, L. E. Brus, T. F. Heinz, J. Hone, and S. Ryu, Anomalous lattice vibrations of single- and few-layer MoS_2, ACS Nano **4**, 2695 (2010).

[33] A. Splendiani, L. Sun, Y. B. Zhang, T. S. Li, J. Kim, C. Y. Chim, G. Galli, and F. Wang, Emerging photoluminescence in monolayer MoS_2, Nano Lett. **10**, 1271 (2010).

[34] B. Chakraborty, A. Bera, D. V. S. Muthu, S. Bhowmick, U. V. Waghmare, and A. K. Sood, Symmetry-dependent phonon renormalization in monolayer MoS_2 transistor, Phys. Rev. B **85**, 161403 (2012).

[35] T. Jin, J. Kang, E. S. Kim, S. Lee, and C. Lee, Suspended single-layer MoS_2 devices, J. Appl. Phys. **114**, 164509 (2013).

[36] K. Kaasbjerg, K. S. Thygesen, and K. W. Jacobsen, Phonon-limited mobility in n-type single-layer MoS_2 from first principles, Phys. Rev. B **85**, 115317 (2012).

[37] Z. Xiao, S. Poddar, S. Ducharme, and X. Hong, Domain wall roughness and creep in nanoscale crystalline ferroelectric polymers, Appl. Phys. Lett. **103**, 112903 (2013).

[38] Z. Xiao, J. Hamblin, S. Poddar, S. Ducharme, P. Paruch, and X. Hong, Effect of thermal annealing on ferroelectric domain structures in poly(vinylidene-fluoride-trifluorethylene) Langmuir-Blodgett thin films, J. Appl. Phys. **116**, 066819 (2014).

[39] C. Jang, S. Adam, J. H. Chen, D. Williams, S. Das Sarma, and M. S. Fuhrer, Tuning the Effective Fine Structure Constant in Graphene: Opposing Effects of Dielectric Screening on Short- and Long-Range Potential Scattering, Phys. Rev. Lett. **101**, 146805 (2008).

[40] K. Zou, X. Hong, D. Keefer, and J. Zhu, Deposition of High-Quality HfO_2 on Graphene and the Effect of Remote Oxide Phonon Scattering, Phys. Rev. Lett. **105**, 126601 (2010).

[41] N. Ma and D. Jena, Charge Scattering and Mobility in Atomically Thin Semiconductors, Phys. Rev. X **4**, 011043 (2014).

[42] M. S. Fuhrer and J. Hone, Measurement of mobility in dual-gated MoS_2 transistors, Nat. Nanotechnol. **8**, 146 (2013).

[43] K. S. Novoselov, D. Jiang, F. Schedin, T. J. Booth, V. V. Khotkevich, S. V. Morozov, and A. K. Geim, Two-dimensional atomic crystals, Proc. Natl. Acad. Sci. U.S.A. **102**, 10451 (2005).

[44] B. Radisavljevic and A. Kis, Mobility engineering and a metal-insulator transition in monolayer MoS_2, Nat. Mater. **12**, 815 (2013).

[45] K. Tashiro, Y. Itoh, M. Kobayashi, and H. Tadokoro, Polarized Raman-spectra and LO-TO splitting of poly (vinylidene fluoride) crystal form-I, Macromolecules **18**, 2600 (1985).

[46] M. V. Fischetti, D. A. Neumayer, and E. A. Cartier, Effective electron mobility in Si inversion layers in metal-oxide-semiconductor systems with a high-kappa insulator: The role of remote phonon scattering, J. Appl. Phys. **90**, 4587 (2001).

[47] J. Kunc, Y. K. Hu, J. Palmer, Z. L. Guo, J. Hankinson, S. H. Gamal, C. Berger, and W. A. de Heer, Planar edge schottky barrier-tunneling transistors using epitaxial graphene/SiC junctions, Nano Lett. **14**, 5170 (2014).